




Research Article

Concurrent Prospects to Develop Activated Charcoal Reinforced Self-Sensing Cement Composites for Structural Health Monitoring Applications

A. Dinesh ¹, D. Suji ², and Moorthi Pichumani ³

¹Department of Civil Engineering, Sri Ramakrishna Engineering College, Coimbatore 641022, India

²Department of Civil Engineering, PSG College of Technology, Coimbatore 641004, India

³Department of Nanoscience and Technology, Sri Ramakrishna Engineering College, Coimbatore 641022, India

Correspondence should be addressed to A. Dinesh; dinesh.a.civil@gmail.com

Received 4 November 2022; Revised 20 February 2023; Accepted 27 February 2023; Published 7 March 2023

Academic Editor: Fabio Casciati

Copyright © 2023 A. Dinesh et al. This is an open access article distributed under the Creative Commons Attribution License, which permits unrestricted use, distribution, and reproduction in any medium, provided the original work is properly cited.

This research examines the electromechanical characteristics of self-sensing cement composite (SCC) containing activated charcoal (AC) at various concentrations (5%, 10%, 15%, 20%, and 25%). The developed composite is placed in various zones in the beam to monitor beam behaviour, as well as in the column center to monitor column deflection. The research reveals that AC reduced the compressive strength and resistivity of cement composites by generating local hydration and carbon accumulation. The performance index approach optimizes AC concentrations at 25% and 20% without and with 10% silica fume (SF), respectively. The embedded SCC has monitored the deflection of beams and columns with a maximum correlation between electrical resistivity and deflection at 99% and 96%, respectively. According to the findings, the AC can generate SCC, which might be utilized to monitor the deflection of beams and columns.

1. Introduction

Engineered cement composites are gaining popularity as nanomaterials emerge that can alter the mechanical and durability qualities of concrete. Despite several material advances, it is still difficult to avoid damage to concrete structures. Monitoring the performance of concrete structures under external loads is called structural health monitoring (SHM) [1–3]. To monitor structural performance, a variety of sensors, such as accelerometers [4], ceramic sensors [5], and fiber optic sensors [6, 7], are available. However, such sensors have limited uses due to their high cost, low sensitivity, and lack of scalability [8]. As a result, a self-sensing cement composite (SCC) that can monitor structural performance is developed [9, 10]. Due to its excellent compatibility and durability, SCC constructed of conductive materials plays a vital part in the SHM compared to traditional sensors. Steel fiber (SF), carbon nanotube (CNT), carbon black (CB), carbon fiber (CF), nickel powder

(NP), and graphite powder (GP) are conductive materials that can help develop the SCC [11–16]. Both fiber and powder materials can develop SCC to detect stress, strain, and damage in concrete structures under monotonic and cyclic loads [17]. It was also revealed that machine learning techniques, such as classification algorithms, can detect independent damage modes in composites with an accuracy of about 95% [18].

Carbon-based materials are utilized in the development of elastomeric isolators, ultra-high-performance concrete, etc., due to their exceptional properties [19, 20]. Carbon-based powder materials have a substantial impact on the advancement of SCC. CB and GP are frequently used in powder-based conductive materials to develop SCC [21]. Monteiro et al. identified that as the CB concentration is higher, the accuracy of resistivity monitoring is higher and showed a maximum reduction in resistivity of 95% ($8 \Omega\text{m}$) at 10% CB [22]. Han and Ou justify the decrease in resistivity by claiming that the integration of CF and CB in the

composite results in a sensitivity of 1.35 MPa^{-1} [23]. Wen and Chung justify the cost-effectiveness of hybrid composites by partially substituting CF with CB, lowering the resistivity to $604 \pm 73 \Omega\text{cm}$ (0.5 CF + 0.5 CB) [24]. Li et al. determined that the addition of nano carbon black results in a negligible reduction of fractional change in resistance (about 2%). However, the fractional change in resistance is increased to 4.6% with the hybrid inclusion of nano carbon black and 0.1% polypropylene fibers due to the adhesion between nano carbon black and polypropylene fibers [25].

Activated charcoal (AC), a highly porous carbon powder that can be synthesized by carbonation, oxidation, or chemical impregnation (such as acid), has been used in cement and concrete for decades [26, 27]. AC is more successful in improving cement strength (=363 psi after one day) and is promising in countering the adverse effects of cement mud contamination [27]. The addition of AC to the concrete mix increased NO_2 absorption ($2.1 \times 10^{-3} \text{ mol/m}^2$ after 24 hours of exposure) without increasing overall porosity or diminishing strength. This is owing to a vast surface area of AC ($695 \text{ m}^2/\text{g}$), which increases the surface area of adsorption and associated chemical reactions [28]. The substitution of acidified AC in cement mortar increased workability by 71.4% due to the plasticizing effect of AC and compressive strength by 9% compared to conventional mortar as a result of local hydration caused by water released from AC pores [29]. The depolluting impact of AC embedded concrete is vital in the face of temperature, humidity, and gaseous pollutants such as formaldehyde and carbon dioxide [30]. Because of the lower void content, AC at 10% lowered the air void content from 10% to 2.1% (increasing freeze-thaw resistance) and enhanced compressive strength from 21.7 MPa to 37.5 MPa. Research has also revealed that the inclusion of carbon content has no adverse effect on the compressive strength of concrete [31]. The strength of concrete with 4% AC is raised to 22.39 MPa from 18.97 MPa (conventional concrete), implying that the addition of AC in the concrete makes the concrete denser and increases the compressive strength [32].

Controversially, the addition of 20%, 30%, and 50% AC lowered the strength of the cement mortar by 10%, 25%, and 40%, respectively [33]. The lower compressive strength is primarily due to a delay in cement particle hydration caused by the pozzolana, which will grow as the AC content increases. The addition of a high proportion of AC necessitates more mixing water due to their high water-absorption capacity, which could reduce the compressive strength of the composite [34]. The porosity of 50% AC mortar is 24%–30% greater than that of conventional cement mortar. Adding 10%, AC to the cement mortar lowered the compressive strength from 36.8 MPa to 27.8 MPa and the tensile strength from 3.24 MPa to 2.55 MPa. The internal curing benefits promoted by hydrated AC and the greater water consumption of AC due to its larger surface area contribute to the reduction in strength [35]. The addition of AC has increased the conductivity inside the cement composite. The AC lowered the resistivity of asphalt concrete containing siliceous particles by 71% and limestone aggregates by 63%, respectively [36]. The AC has a propensity to decrease thermal conductivity (1.52 W/mK) and increase specific heat in the composite

(0.84 KJ/kgK) due to the lower density and heat capacity of paraffin (2 KJ/kgK) used in the research [37]. The AC is also used to remove organic contaminants from the water, with methylene blue and rhodamine adsorptive removal rates of 80% and 71%, respectively [38].

Because of the rough texture of the activated carbon utilized, it can be used as a partial replacement for aggregate, increasing the strength of concrete by up to 50 MPa. A similar pattern is found in splitting tensile strength, where the increase in strength ranges from 25% to 60%. Due to the presence of internal fissures between paste and aggregates, the depth of water penetration is between 5 mm–24 mm [39]. The flexural strength of the powder-activated carbon (PAC) embedded concrete was raised from 3.30 MPa to 3.59 MPa (0.75% PAC) [40]. A modest concentration of regenerated activated carbon contributes to the quick adsorption of phenol-contaminated sand during the solidification/stabilization process (1%–2% wt. of sand) [41]. In addition to a Macro Defect Free (MDF) cement incorporating vinyl polymer, activated carbon produces a moisture-blocking, long-lasting cement material [42]. A hybrid combination of activated carbon powder, hollow glass microspheres, and carbon nanofibers is employed in lightweight engineered cementitious composites [43].

Thus, the AC is evaluated mainly for its impact on composite strength alterations of cement composite. The AC embedded cement composite is monitored in terms of durability (temperature, humidity, organic contaminants), thermal conductivity, specific heat, and other factors. While research studies are conducted on AC embedded cement composite for mechanical and thermal properties, the suitability of AC embedded composites for conductive and sensing properties of cement composite is unexplored. This study determines that AC can develop an SCC with a high conductivity ($=114 \Omega\text{cm}$) and piezoresistivity (about 8%). Additionally, this research optimizes the electromechanical properties of AC embedded SCC, with morphological analysis to justify the property enhancement. Furthermore, to enable the real-time application of the developed SCC, the SCC was embedded in reinforced concrete beams and columns, and it is determined that the resistivity variation of SCC in beams and columns has a 99% (approx.) and 96% (approx.) correlation with deflection, respectively. The objective of this research is to (a) measure the compressive strength, conductivity, piezoresistivity, and stress sensitivity of SCC at various AC concentrations without and with 10% silica fume (SF), (b) optimize the SCC using a performance index that considers both mechanical and electrical characteristics, (c) characterize the microstructure of cement composites using scanning electron microscopy (SEM), X-ray diffraction (XRD), and energy dispersive X-ray (EDAX) investigations, and (d) apply the developed SCC in various zones of beams and columns to monitor deformation through changes in electrical resistivity of embedded SCC.

2. Materials

The conventional cement composite comprises ordinary portland cement (OPC) grade 53, natural sand, and SF from

ASTRRA Chemicals, Chennai, India. The chemical composition of cement (calcium = 63.288%), fine aggregate (silica = 77.626%), and SF (silica = 96.279%) is determined by XRF analysis. IS 4031 (Part 11) is used to measure the specific gravity of cement (=3) and SF (=2.64), whereas IS 2386 (Part 3) is used to determine the specific gravity of sand (=2.717). Master Sky Glenium from ASTRAA Chemicals, India, with a pH of 6 and a specific gravity of 1.10, is utilized as a chemical additive to enhance the workability of the SCC. To improve the electrical characteristics of the composite, the AC (Model: LOBA Chemie) from RB Scientific, Coimbatore, India, is utilized. Table 1 summarises the physical characteristics of AC.

EDAX analysis is used to identify the chemical composition of AC, as presented in Table 2. The carbon content of AC has been calculated to be 87.05%. AC, as depicted in Figures 1(a) and 1(b), and it takes priority in this research because the carbon content controls the conductivity [44]. Four copper meshes measuring 70 mm in width, 50 mm in depth, and 1 mm in breadth are utilized to evaluate the electrical characteristics of the cement composite using the four-probe method.

The cementitious material-sand ratio and the water-cement ratio of cement composite are maintained at 1 and 0.3, respectively. AC is a novel substance that has been utilized to create an SCC. Since AC is a powdered substance with low carbon content, it is used in concentrations ranging from 5% to 25% by weight of the binder, with a 5% increase [45]. SF, which was employed in previous research studies to improve material dispersion, is included in this study at 10% of the weight of the binder. SF, due to its small size, is good at separating conductive particles during the mixing process and enhancing AC dispersion [46]. The various mix proportion used to develop SCC is shown in Table 3. The surface area of the composite grows as the AC concentration rises, resulting in water scarcity. As a result, the superplasticizer concentration in the composite is changed between 1% and 2% to maintain the workability of the composite (=230 mm) constant. As defined by IS 2250-1981, the flow table experiment is used to measure the workability of SCC.

Cement, sand, and SF are mixed for 60 seconds before integrating into the AC embedded cement composite. Then, 2/3 of the water and superplasticizer should be stirred for 120 seconds in a flask before mixing with the dry materials for 60 seconds. The remaining 1/3 of the water is added to AC and swirled gently for 120 seconds before being vigorously agitated for another 120 seconds. The solution is then mixed for 60 seconds with the premixed dry components. Finally, the mix is poured into the specially prepared lubricated mould, and the electrode is inserted simultaneously. The spacing between the internal electrodes is preserved at 20 mm, while the gap between the inner and exterior electrodes is kept at 10 mm. The specimens are demoulded after 24 hours and water cured for 28 days.

3. Methods

In compliance with IS 4031 (Part-6), the compressive strength of the SCC is assessed using a 200T capacity

TABLE 1: Physical properties of AC.

AC	
Property	Value
Colour	Black
State	Solid
Vapour density	0.4
Density (g/cc)	1.8–2.1
Particle size (mm)	0.25
Electrical conductivity (S/cm)	2.4×10^{-7}
pH value	6–9

TABLE 2: EDAX analysis of AC used to develop SCC.

Element	3 sigma (weight%)	Norm C (weight%)
Carbon	31.64	87.05
Oxygen	8.05	12.95

compressive testing machine (AIMIL-AIM 317E-AN). A power supply unit (PSU) applies DC to the two outside current electrodes. A multimeter (fluke 15 b) is employed to monitor the voltage between the two inner current electrodes simultaneously. The formula $R = V/I$ is used to calculate the resistance (R) value, where V denotes the voltage, and I represents the current supplied to the electrodes of SCC. Resistivity ($\rho = RA/L$) is calculated to consider the geometry of the composite, where A denotes the area of the SCC and L represents the spacing between the two voltage electrodes. The initial resistivity, stress, and resistivity during load application are simultaneously calculated. The FCR is computed by the equation as follows:

$$FCR = \frac{\rho - \rho_0}{\rho_0}, \quad (1)$$

where ρ indicates the resistivity at each load increment, and ρ_0 exhibits the initial resistivity of SCC. Stress sensitivity is computed using the formula FCR/σ , where σ denotes the longitudinal stress of the SCC. The stress (σ) of the composite is calculated using the formula $\sigma = P/A$.

For microstructural analysis, a Field Emission Scanning Electron Microscopy (FESEM) system (Make: CARL ZEISS (USA), resolution = 1.5 nm) is employed. The XRD test on the composite is conducted at 30 mA and a scanning range of 5 to 90° (=2 θ). The elemental constituents of optimized powdered SCC are determined using EDAX analysis (Make: Bruker, Model: Nano XFlash detector). The diffraction angle used in the test ranges from 0 to 90°.

RCC beams of effective span 1.5 m (clear span = 1.8 m, breadth = 0.15 m, and depth = 0.25 m) are cast with embedded SCC to determine its flexural strength. The concrete is cast for M20 grade as per IS 10262:2009, and the reinforcements are designed in accordance with IS 456:2000. The beam reinforcements are designed using Fe415 reinforcements with a yield strength of 240 MPa.

The flexural strength of the beam is determined by applying a two-point load with a 100 T (UNITECH) loading frame. According to the mechanics, the beam is divided into three zones, with the center span subjected to pure flexure and the end spans subjected to a combination of flexure and



FIGURE 1: Illustrations of (a) AC-video camera and (b) AC-SEM.

TABLE 3: Mix proportion of SCC developed using AC.

Mix ID	SF (wt. of cement)	AC (wt. of cement)
C	—	—
5% AC	—	0.05
10% AC	—	0.10
15% AC	—	0.15
20% AC	—	0.20
25% AC	—	0.25
C-SF	0.1	—
5% AC-SF	0.1	0.05
10% AC-SF	0.1	0.10
15% AC-SF	0.1	0.15
20% AC-SF	0.1	0.20
25% AC-SF	0.1	0.25

shear [46]. Hence, SCC is positioned at the center top (uniaxial compression), center bottom (uniaxial tension), and 500 mm from the middle of the beam (combined flexure and shear), as depicted in Figure 2. A linear variable differential transformer (LVDT) with a sensitivity of 0.001 mm and a dial gauge are used to detect beam deflection at the center and 500 mm from the center of the beam, respectively.

By applying an axially compressive force, the deflection of a column (height = 1 m, width = 0.15 m, and depth = 0.50 m) with SCC placed in the core is determined. A 100 T (UNITECH) loading frame is used to apply a compressive force to the column. Using an LVDT, the vertical deformation of the column is monitored. The column is cast for grade M20 according to IS 10262:2009. The column reinforcements are designed using Fe415 reinforcements as per IS456:2000.

4. Results and Discussion

4.1. Compressive Strength. Figure 3 depicts the compressive strength of SCC with various proportions of AC without SF and with 10% SF. The standard deviation of strength for all the mixes is between 0.10 MPa and 0.55 MPa. The coefficient of variation for strength ranges from 0.6% to 2.4%. The strength of the SCC decreases as the proportion of AC in the SCC increases. As shown in Figure 3, the compressive strength is reduced by 9.65%, 19.37%, 35.49%, 39.44%, and 43.27% when 5%, 10%, 15%, 20%, and 25% AC is added, respectively. The findings are consistent with earlier studies.

According to Li and Li, 5% CB reduces compressive strength by 27%, whereas 10% CB reduces compressive strength by 32% [47]. Dong et al. also show a decrease in strength by 32.7%, 56.4%, and 72.7% for 1%, 2%, and 4% CB, respectively [34]. Monteiro et al. show a reduction in compressive strength of 9% at 10% CB [48].

Since the use of AC in the fabrication of SCC is a unique idea, earlier research in GP and CB (carbonaceous powder particles comparable to AC) is utilized to discuss the results (compressive strength, resistivity, piezoresistivity, and stress sensitivity). The internal curing advantages supported by the hydrated AC and the increased water consumption of AC owing to its larger surface area contribute to the decline in strength [35]. The AC absorbs water and binds to the cement surface, slowing down the hydration process, and resulting in reduced compressive strength of the SCC [34]. The decrease in strength is also due to the surface energy of AC particles, which causes AC to agglomerate together and form clusters [34]. Similar to GP [49], the smooth surface of AC, as observed in Figure 1(b), the difference in hydrophilicity of cement and AC [49], and the increased water consumption of AC [50], lead to the decline in the strength of SCC.

As depicted in Figure 3, the addition of 10% SF increases the compressive strength of all composites, both with and without AC. When 10% SF is incorporated into the conventional cement composite, the strength improves by 16%. Incorporation of 10% SF composite shows an increase in strength by 3.33%, 5.04%, 13.85%, 22.35%, and 30.19% in 5%, 10%, 15%, 20%, and 25% AC-SF composites, respectively, compared to AC alone incorporated cement composite. The pozzolanic reaction and reduced particle size of SF increase the packing density and modify the pore structure of the composite, resulting in a densified cementitious microstructure [47]. According to prior studies, the creation of C-S-H crystals generated by SF and the pore-filling capability of SF in the cement composite also contribute to the strength amplification of AC-SF composites [51, 52].

4.2. Electrical Properties

4.2.1. Electrical Resistivity. The fluctuation of resistivity at various concentrations of AC without and with 10% SF is shown in Figure 4. The standard deviation of resistivity

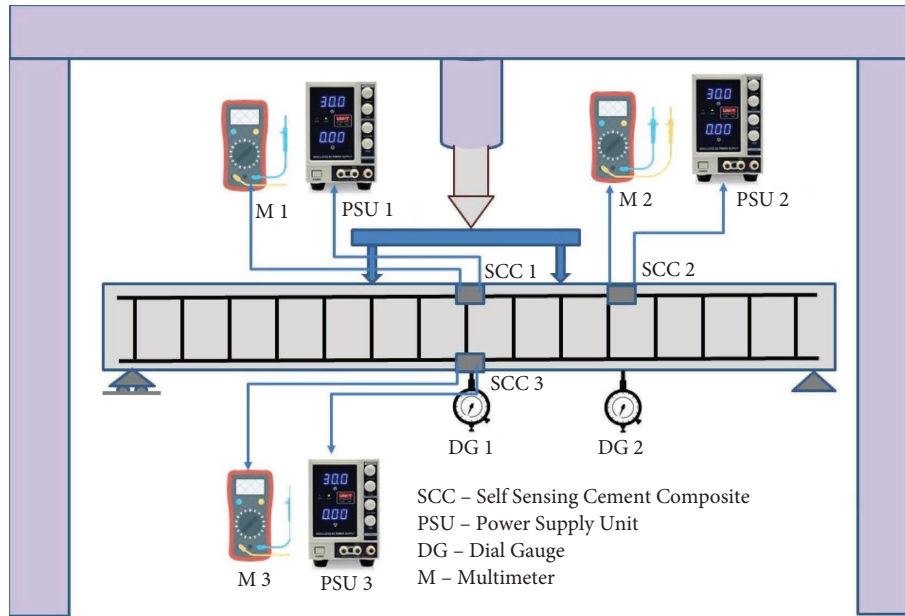


FIGURE 2: Research setup for concurrent measurement of beam deflection and SCC resistivity.

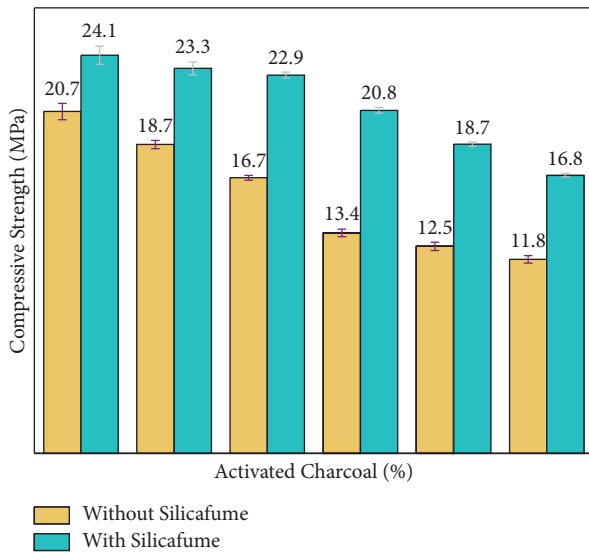


FIGURE 3: Strength of AC integrated SCC including and excluding SF.

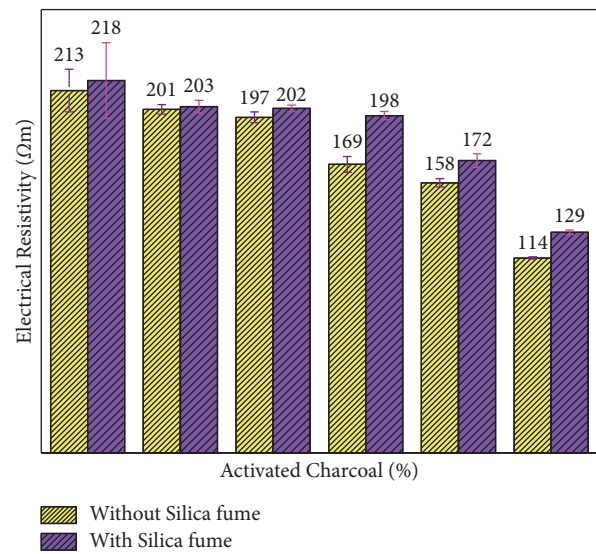


FIGURE 4: Resistivity of AC integrated SCC including and excluding SF.

ranges from 0.069 Ωm to 2.22 Ωm. The coefficient of variation of electrical resistivity for AC embedded composites varies between 0.6% and 10.17%. As presented in Figure 4, the decrease in resistivity is proportional to the increase in AC concentration. From Figure 4, it is observed that the electrical resistivity is reduced by 5.20%, 7.37%, 20.37%, 25.45%, and 46.20% for 5%, 10%, 15%, 20%, and 25% of AC inclusion, respectively. Similarly, the resistivity is reduced by 7%, 7.48%, 9.41%, 21.47%, and 40.76% for 5%, 10%, 15%, 20%, and 25% of AC-SF inclusion, respectively. The findings are comparable to the research of Dong et al. who found that at 2% CB, electrical resistivity drops by 85%. The more significant reduction in resistivity is primarily due to the

high purity carbon content (>99.5%) in the CB utilized in the composite development. Li et al. discovered that including CB reduces electrical resistivity from 10000 Ωcm (5 wt. of cement) to 100 Ωcm (10% wt. of cement). At lower AC concentrations (201 Ωcm for 5% AC and 203 Ωcm for 5% AC-SF), the resistivity values are high. This is because the conductive AC will be negligible in the SCC compared to the hydration products (C-S-H, Portlandite, and Ettringite-refer to Section 4.4.1). As a result, the hydration products act as barriers, preventing the composite from forming a continuous conducting network [53]. However, as the AC concentration increases, the electrical resistivity decreases significantly (114 Ωcm for 25% AC and 129 Ωcm for 25% AC-

SF) due to the creation of more conductive networks in the composite [54]. The resistivity fluctuations in the composite are influenced by the concentration of AC and the quality of connections between AC [55].

From Figure 4, it is understood that the inclusion of SF increases the resistivity by 0.81%, 2.65%, 16.92%, 8.26%, and 13.16% at 5%, 10%, 15%, 20%, and 25% of AC-SF embedded cement composite, respectively, compared to the AC alone embedded cement composite. The presence of SF in the composite densifies the matrix by developing additional hydration products (C-S-H), which act as a barrier and lead to a substantial increase in the resistivity of the composite [34] (Refer XRD analysis-Section 4.4.3).

The percolation threshold for CB-induced cement composite is 7.22–11.39% by Li et al. [54]. Wu et al. reported that the percolation threshold for GP and CB is 10% and 12%, respectively [53]. According to our findings, the electrical resistivity of AC embedded composites does not vary substantially till 10%. However, there is a considerable drop in resistivity in AC alone embedded cement composites from 7.37% (10% AC) to 20.37% (15% AC). Similarly, in the AC-SF embedded cement composite, there is no substantial resistivity fluctuation until 15% (9.41%). However, at 20% AC-SF and 25% AC-SF, the resistivity is reduced by 21.47% and 40.76%, respectively. This demonstrates that the percolation threshold is 15% for AC embedded composite and 20% for AC-SF embedded composite. Because of the significant distance between porosities, electrons take a long time to flow through SF embedded composites, delaying polarisation, and the formation of the percolation threshold in AC-SF composites [56].

4.2.2. Piezoresistivity. Figure 5 depicts FCR vs. stress for an AC integrated SCC without SF. The FCR value is initially lowered for all % of AC embedded composite with an increase in stress (reduced till 12 MPa for 5% and 10% AC, 8 MPa for 15% AC, 10 MPa for 20% AC, and 6 MPa for 25% AC). For 10% AC, the minimal reduction in FCR is 4.30%, which might be attributable to low concentration and accumulation of AC. For 25% AC, the most significant decrease in FCR (5.70%) is obtained. This is because, with more excellent AC, more clusters in the cement composite are close to each other (supported by SEM analysis-refer to Section 4.4.1). As the load increases, fewer AC moves closer to each other, contributing to tunneling conduction, and fewer AC comes into contact, contributing to composite contact conduction [17].

For all % concentrations of AC, the FCR value increases after a given stress value due to material breakage. However, the stress value at which the FCR increases varies due to changes in the compressive strength of composite with different% of AC. It is evident from Figure 5 that the high concentration of AC composites attained their maximal resistivity reduction with a smaller stress increment. It is worth noting that while using 25% AC, the FCR is reduced to 5.70%, and its ability to diminish resistivity with increasing stress (i.e., its applicability in concrete structure health monitoring) is restricted at a lower stress value (6 MPa).

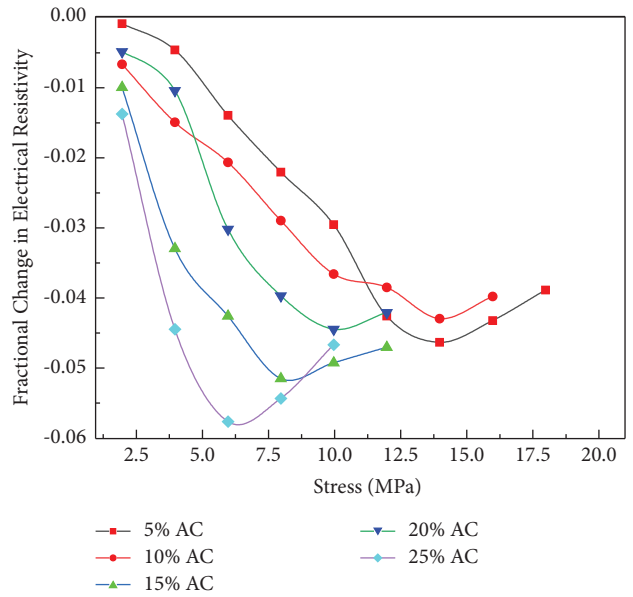


FIGURE 5: FCR vs. stress for AC integrated SCC excluding SF.

However, SCC can reduce resistivity until 14 MPa despite the fact that 5% AC can lower the FCR to 4.63% only. Thus, compressive strength and conductivity are required to make the SCC have long-term usage in the health monitoring of structural components.

In AC embedded cement composite with SF, the FCR fluctuation concerning stress is shown in Figure 6. A linear decrease in FCR is observed with increasing stress at 5%, 10%, and 15% AC-SF composites. They have a high compressive strength, which prevents the composite from breaking. The maximum reduction in FCR is observed as 4.69%, 5.29%, and 8.18% in 5%, 10%, and 15% AC-SF composites. Thus, until 15% AC inclusion, the magnitude of the maximum reduction in FCR is proportional to the amount of AC in the composite. The higher the AC, the more conductive network is developed in the SCC during the application, resulting in a lower FCR in the composite. The compressive strength is lowest in 20% AC and 25% AC. Therefore, the FCR decreases until it reaches its elastic regime, after which it increases owing to the creation of cracks. For 25% AC, the decline in FCR is limited to 6.56% (=12 MPa) owing to SCC failure. Thus, the reduction in FCR in the composite is determined not just by the concentration of AC but also by the strength of the composite.

4.2.3. Stress Sensitivity. Figure 7 shows the stress sensitivity of an AC integrated SCC without SF as a function of stress. Figure 7 indicates that the stress sensitivity value initially increases for all concentrations of AC (increased to 14 MPa for 5%, 4 MPa for 10% AC, 15% AC, 20% AC, and 25% AC). The increased stress sensitivity results from the high absorption capacity of AC, which generates clusters as the load increases [57]. The stress sensitivity of 5% AC is enhanced till a stress of 14 MPa due to the high compressive strength and low AC content. Since the concentration of AC is minimal, the conductive channels are formed at higher stress levels.

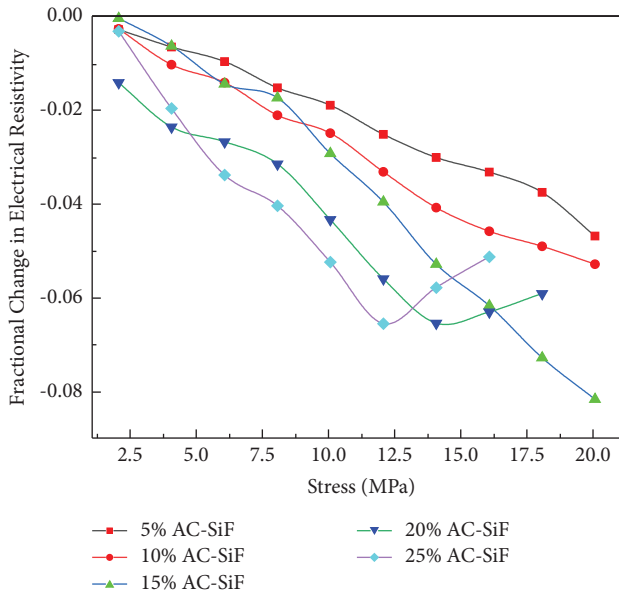


FIGURE 6: FCR vs. stress for AC integrated SCC including SF.

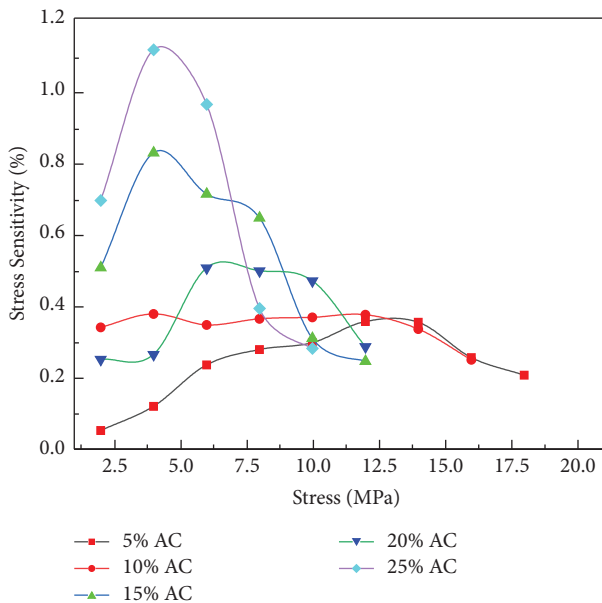


FIGURE 7: Stress sensitivity vs. stress for AC integrated SCC excluding SF.

Consequently, contact conduction and tunneling conduction contribute to a significant decrease in resistivity and an enormous increase in stress sensitivity at a higher level of stress. Besides, maximum stress sensitivity of 1.1% is achieved in a 25% AC embedded cement composite. This is because, in addition to cluster formation (as observed in 5% AC), a continuous conductive channel is formed in 25% AC embedded composite (due to the high concentration), resulting in a significant increase in the sensitivity of the SCC when compared to other concentrations [58]. However, the stress sensitivity diminishes below 4 MPa at 25% AC, showing that the composite is inefficient at higher stress values.

Figure 8 represents the stress sensitivity of an AC embedded cement composite with SF as a function of stress. The stress sensitivity of 10%, 15%, and 25% AC-SF composites increases to around 0.35%, 0.25%, and 0.55% at 6 MPa due to the good dispersion of AC by SF. With an increase in load, AC forms conductive channels and permits electron flow through the channels, resulting in the development of contact and tunneling conduction, which contributes simultaneously to the decreased resistivity and increased stress sensitivity at lower stress levels. However, there is a slight variation in stress sensitivity (0.45% at 2 MPa to 0.4% at 20 MPa) for 5% AC-SF embedded cement composite. This is because, at lower concentrations of AC-SF (5%), there is a good dispersion of AC by SF, which causes only a slight fluctuation in AC orientation as the stress level increases, resulting in a slight variation in stress sensitivity. The maximum strain sensitivity is around 0.7% for 20% AC-SF composite than 25% AC-SF composite, which is in agreement with an investigation by Li et al. [54]. The stress sensitivity decreases until it reaches 8 MPa for 20% AC, indicating a significant agglomeration of AC in the composite and conductive network disruption by the SF particles.

4.3. Performance Index. An SCC must possess high electromechanical properties to monitor the structural components successfully. The performance index (PI) technique, a management tool that integrates several data sets, is utilized to optimize SCC [13, 58]. If the primary requirement for a cement composite is strength, PI 1 should be used. If both strength and conductivity are required, PI 2 is preferred. PI 3 is recommended if strength, conductivity, and piezoresistivity are necessary. If strength, conductivity, piezoresistivity, and stress sensitivity are required, then PI 4 is preferred.

Initially, the weight ranking (Wr) is calculated by multiplying the measured performance of each mix by the best version of all the combinations; for example, the compressive strength of each mix is divided by the maximum compressive strength. The composite with the best performance is given a value of 1, as shown in Figure 9, while the others are given a value of <1. As shown in Figures 9(a) and 9(b), 5% AC and 5% AC-SF have a value Wr of 1, respectively, indicating that those composites have the highest compressive strength.

Wr is multiplied by 5 to get the numeric index (Ni). Ni=5 will be assigned to the composite with the best performance, and Ni for the remaining composites will be proportioned to the best value, 5, as depicted in Figures 10(a) and 10(b). As indicated in Figures 10(a) and 10(b), 5% AC and 5% AC-SF have a value Ni of 5, respectively, indicating that those composites have the highest strength.

Finally, the Ni is calculated for each ID and divided by the best numeric index. The performance index of each ID is calculated as a percentage of the total value, with 100 representing the best performance. The performance index for AC and AC-SF embedded cement composites is shown in Figures 11(a) and 11(b). As observed in Figures 11(a) and 11(b), the best % inclusions are 25% AC and 20% AC-SF, respectively.

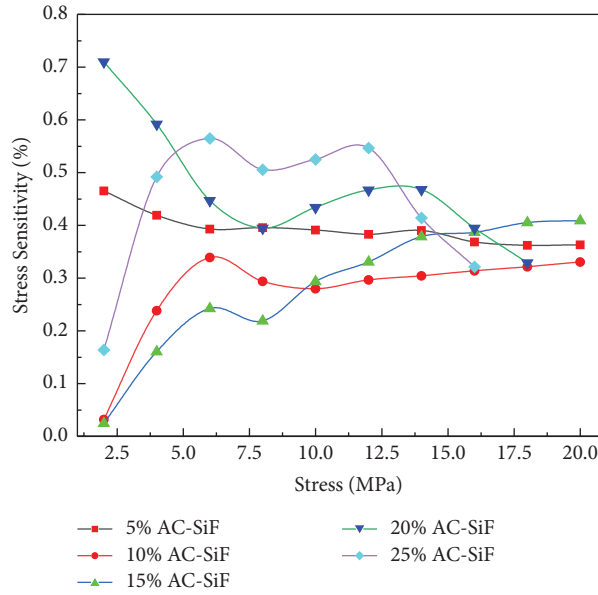


FIGURE 8: Stress sensitivity vs. stress for AC integrated SCC including SF.

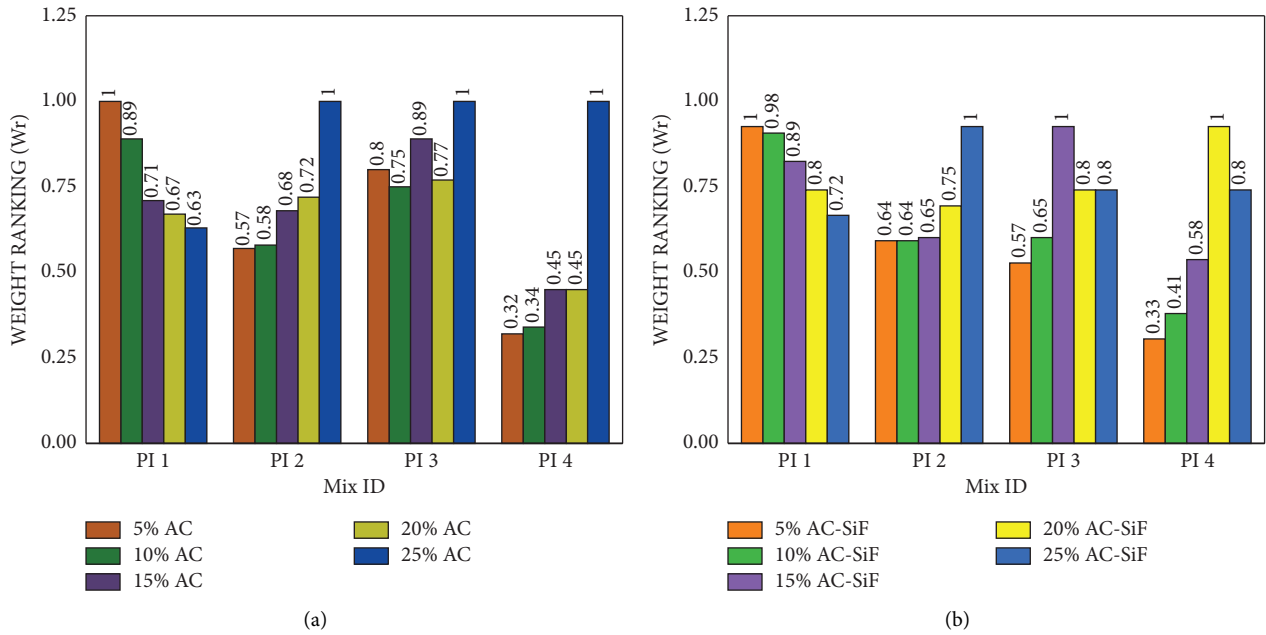


FIGURE 9: Weight ranking of AC and AC-SF embedded cement composite.

The piezoresistivity and stress sensitivity of optimized cement composites (25% AC and 20% AC-SF) are shown in Figures 12 and 13. Figure 12 shows a polynomial curve ($ax^2 + bx + c$) that can fit the relationship between FCR and stress for all suitable cement composites. According to previous research, as shown in Figure 12, the R^2 value for all ideal cement composites is more significant than 0.93 ($0.9643 = 25\% \text{ AC}$ and $0.9315 = 20\% \text{ AC-SF}$), indicating that the polynomial equation may be used to detect FCR [59].

In stress sensitivity vs. stress curve, as shown in Figure 13, the polynomial fit sets excellent for 25% AC and 20%

AC-SF composites with $R^2 > 0.76$, implying that those curves may be used to determine the stress sensitivity roughly, indicating that the polynomial equation may be employed for stress sensitivity detection.

4.4. Morphological Characterization. To establish the causes for the property enhancement in the composite, SEM, XRD, and EDAX are used to analyze the morphological characteristics of the cement composites (25% AC and 20% AC-SF) optimized using the PI technique.

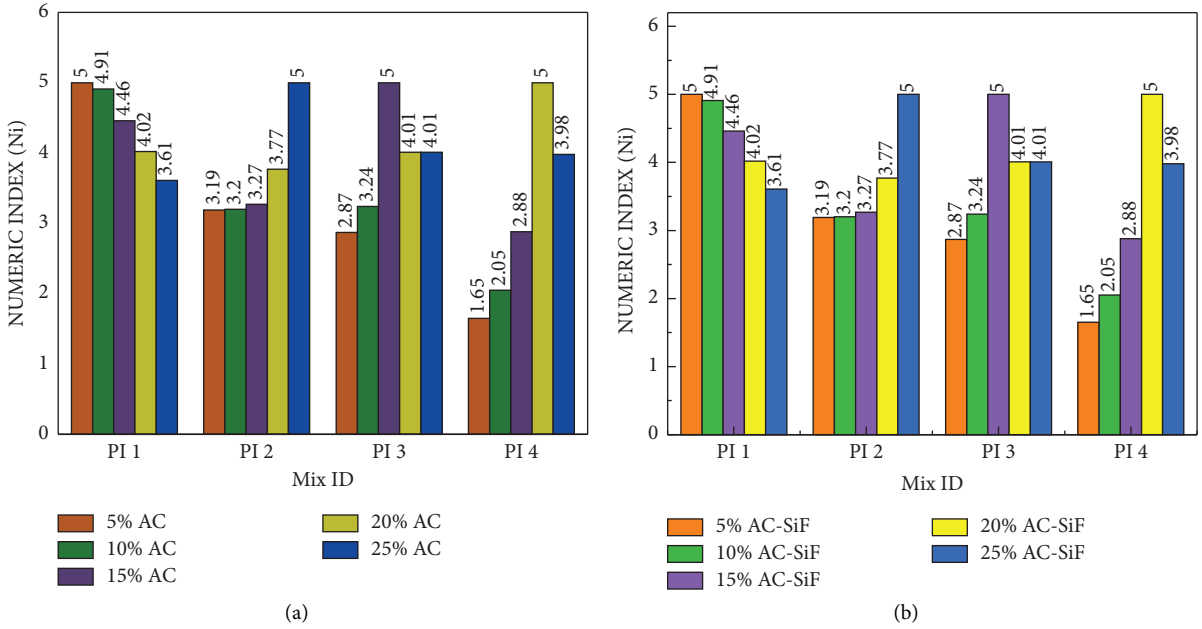


FIGURE 10: Numeric index of AC and AC-SF embedded cement composite.

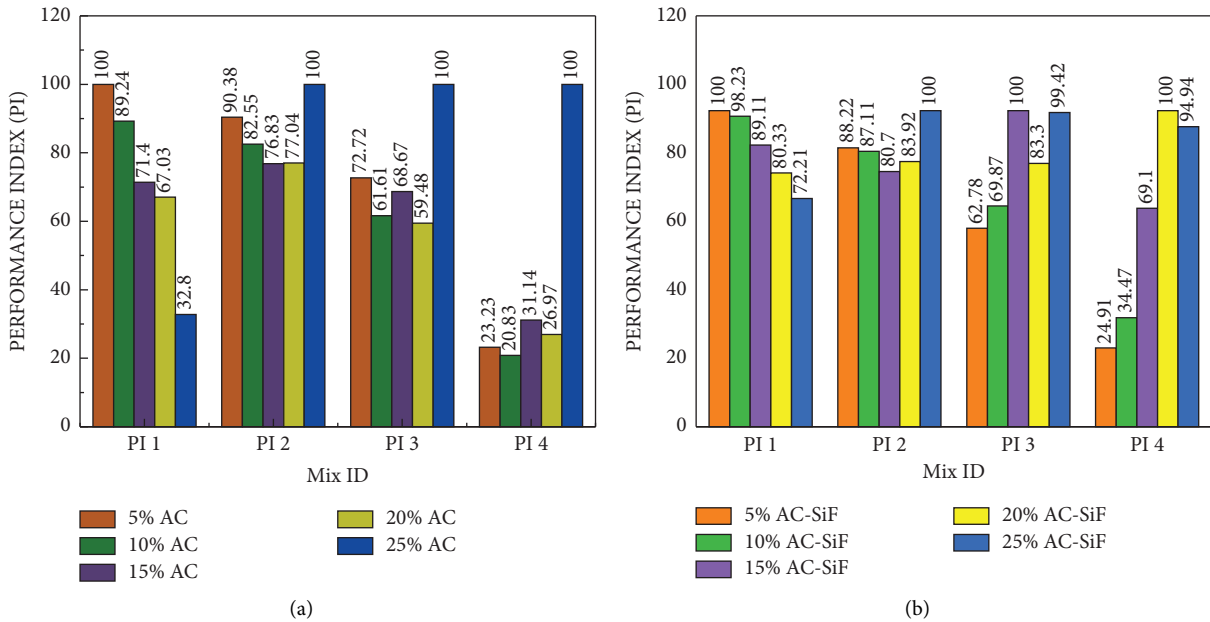


FIGURE 11: Performance index of AC and AC-SF embedded cement composite.

4.4.1. SEM Analysis. Figure 14 shows an SEM image of AC embedded cement composite at different scales ($2\mu\text{m}$, $1\mu\text{m}$, and 300nm). The presence of hydration products (C-S-H , Ca(OH)_2 , and Ettringite) is verified in Figures 14(a)–14(d). The increased number of C-S-H randomly distributed throughout the composite, as observed in Figure 14(a), increases the strength of the composite. The cement composite has AC clusters, as depicted in Figure 14(a), and continuous AC, as shown in Figure 14(c), which contributes to the lower resistivity of the composite.

On the other hand, the cementitious products formed between AC intervene as a barrier for conductivity augmentation in the composite, as shown in Figure 14(a) (discussed in Section 4.2.1). The AC in Figures 14(b) and 14(c) is in close proximity to one another. When a load is applied to the composite, these AC may contact one another, causing contact conduction and tunneling conduction in the SCC. When a load is applied, these conduction help to reduce the FCR and increase sensitivity. As depicted in Figure 14(d), the strength of the AC embedded cement composite is lowered because of the bigger pores and more ettringite formation.

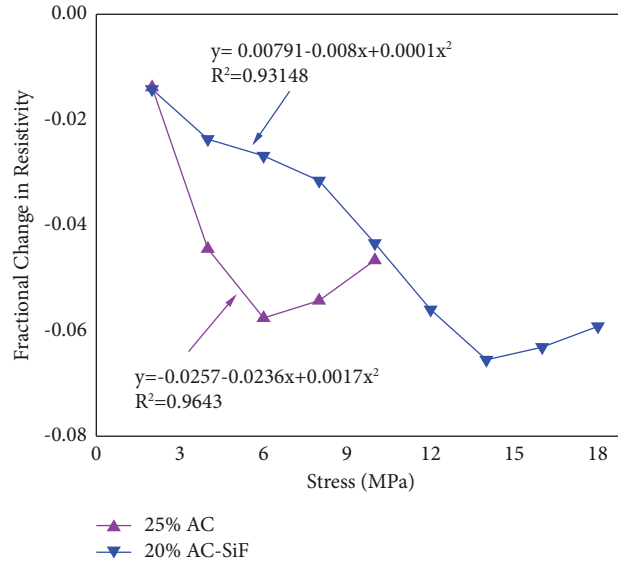


FIGURE 12: FCR vs. stress of optimized cement composites (25% AC and 20% AC-SF).

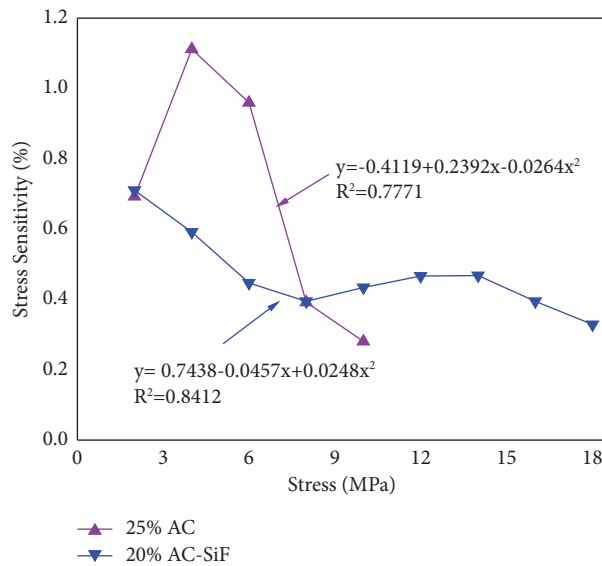


FIGURE 13: Stress sensitivity vs. stress of optimized cement composites (25% AC and 20% AC-SF).

Figures 15(a)–15(d) show SEM images of AC-SF embedded cement composite at different scales (2 μm and 200 nm). As illustrated in Figures 15(a) and 15(d), the growth of C-S-H and $\text{Ca}(\text{OH})_2$ in the cement composite contributes to the strength of the composite. Figure 15(b) depicts the formation of continuous AC in the composite, which leads to contact and tunneling conduction. As shown in Figure 15(b), the existence of a cluster of AC, C-S-H, and $\text{Ca}(\text{OH})_2$ in the cement composite suggests that the AC does not react with the cementitious components and instead forms a continuous conductive network that promotes the decrease in resistivity of the SCC. Figure 15(c) displays the porosity and ettringite formation in the composite, both of which contribute to the strength deterioration in the SCC.

4.4.2. *EDAX Analysis.* Figure 16(a) shows the dominant peak of carbon (C) (=38.66%) in EDAX analysis. In contrast, Figure 16(b) shows the reduced C content (=23.66%) due to the inclusion of SF content in the cement composite, indicating that the correct mix of materials is employed for electromechanical assessment in the composite. Similarly, the silicon (Si) concentration in 25% AC-SF (11.83%) is higher than in 20% AC (=4.81%). The extra Si in the SCC aids in converting portlandite to C-S-H, resulting in higher strength (max. of 30.89%) in SCC, as described in Section 4.1. Due to the extra Si, more C_3S and C_2S are formed, helping the early strength growth in the composite. The Si content of the 20% AC embedded composite is low, as shown in Figure 16(a), justifying the lower strength in the AC embedded SCC (as discussed in Section 4.1).

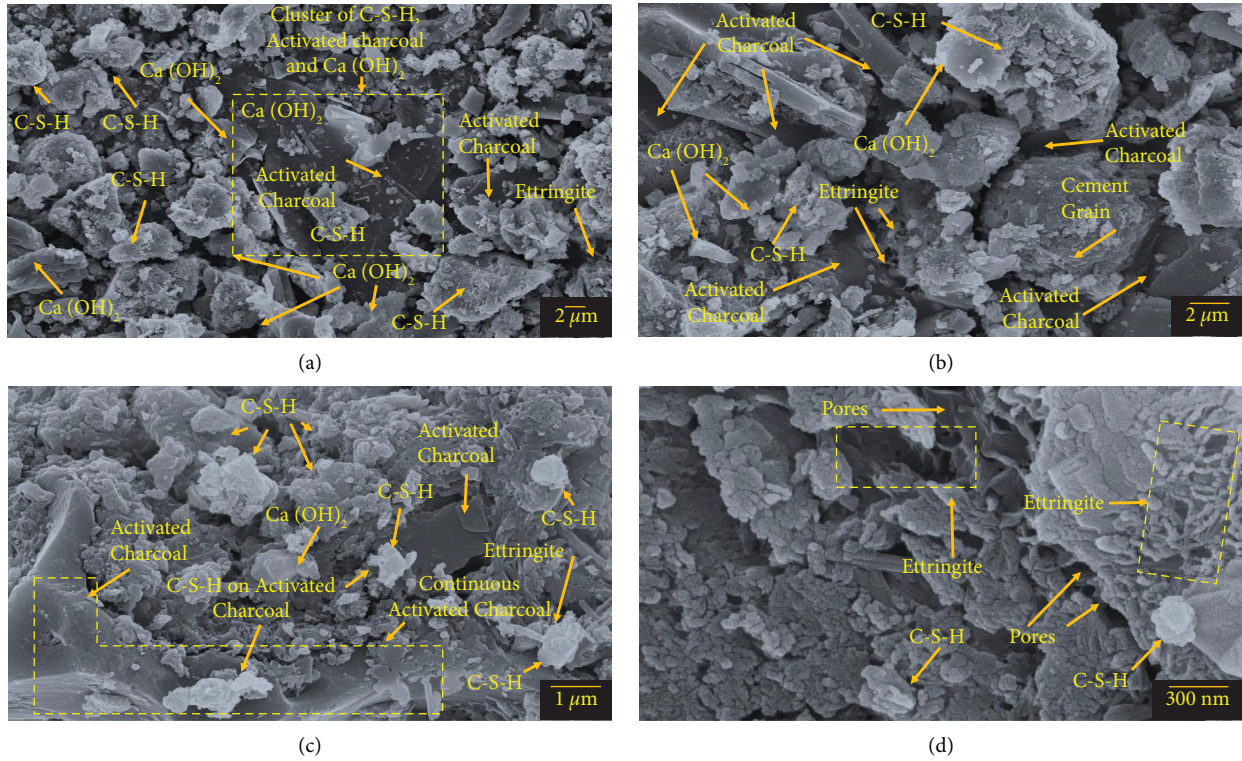


FIGURE 14: SEM images of AC integrated SCC: (a) 2 μm scale, (b) 2 μm scale, (c) 1 μm scale, and (d) 300 nm scale.

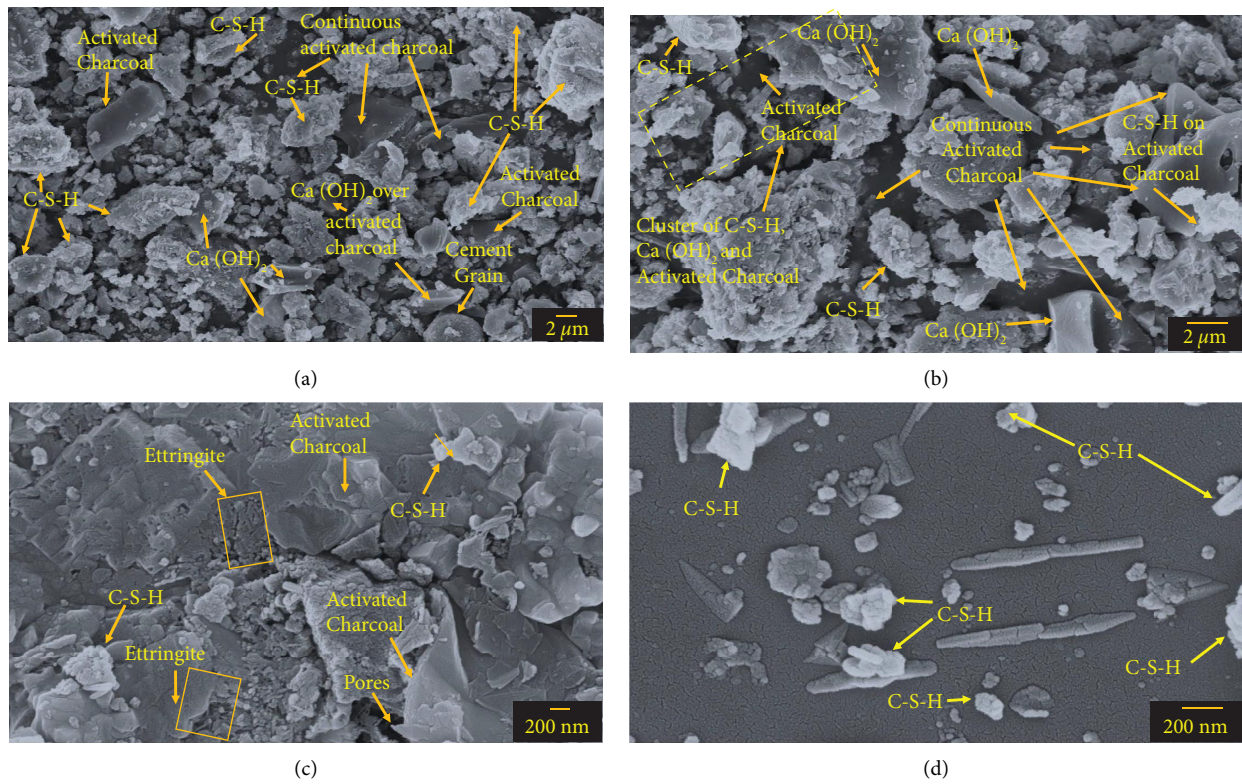


FIGURE 15: SEM images of AC-SF embedded cement composite: (a) 2 μm scale, (b) 2 μm scale, (c) 200 nm scale, and (d) 200 nm scale.

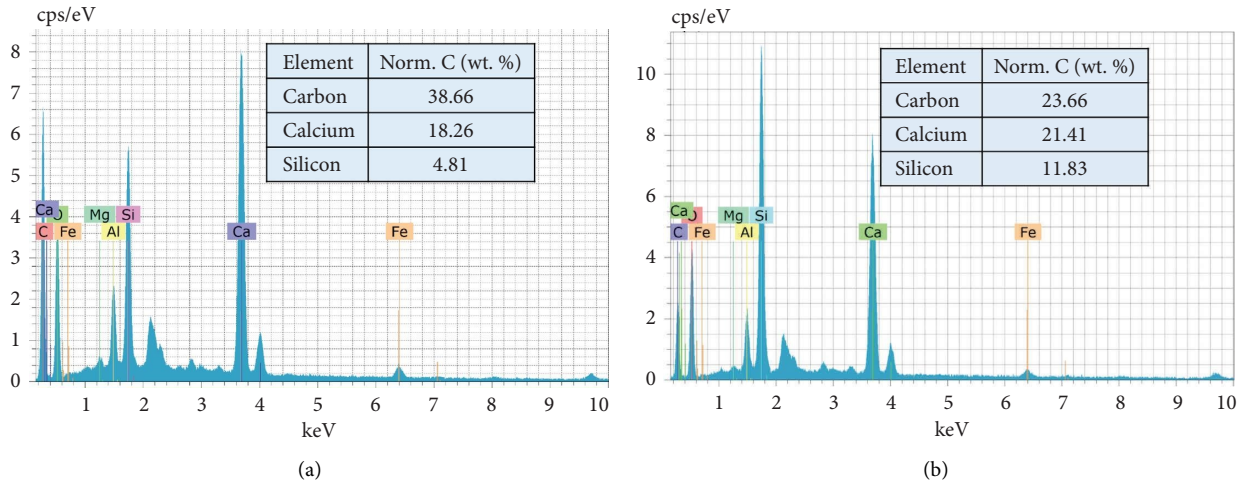


FIGURE 16: EDAX analysis of (a) AC integrated SCC and (b) AC-SF integrated SCC.

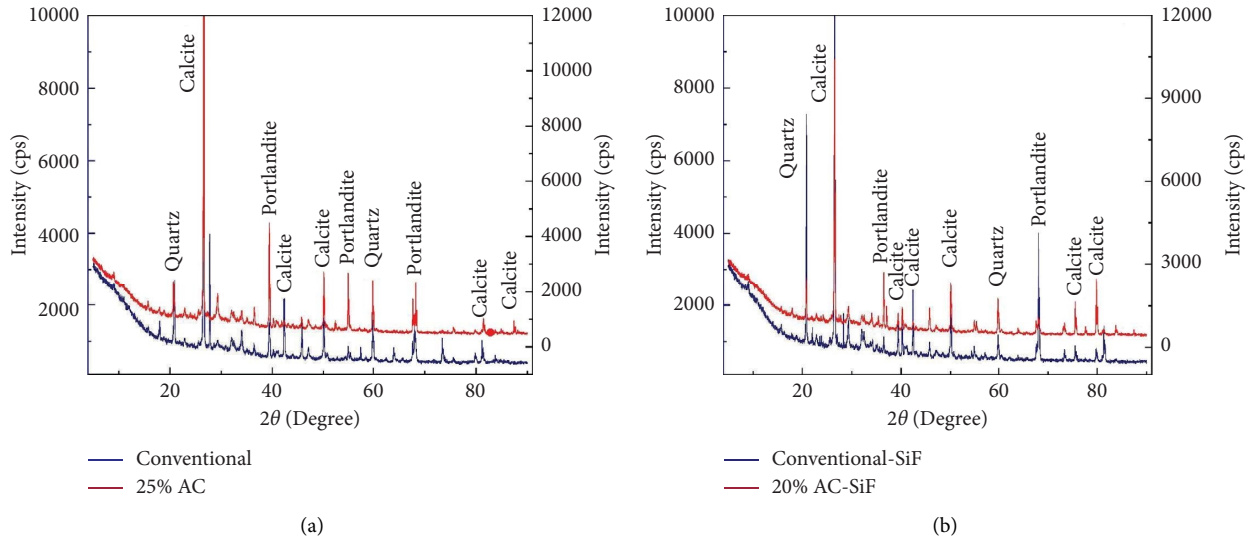


FIGURE 17: XRD analysis of conventional composite with (a) AC integrated SCC and (b) AC-SF integrated SCC.

4.4.3. XRD Analysis. Figure 17 shows XRD studies of (a) AC integrated SCC and (b) AC-SF integrated SCC. The phases detected by XRD analysis are in agreement with previous research [60]. Figure 17(a) depicts the crystallinity changes of conventional cement composite and 25% AC embedded cement composite. The most prevalent hydration products in conventional and 25% AC embedded cement composites are quartz, portlandite, and calcite. The formation of portlandite and calcite is shown by SEM analysis also (refer to Section 4.4.1 and Figures 14(a)–14(d)), suggesting that the cement composite is completely hydrated.

The calcite created in the 20% AC-SF embedded cement composite is equivalent to that of the AC embedded cement composite. Also, in 20% AC-SF embedded cement composite, the quantity of quartz and portlandite formed is high (mainly due to the contribution of SF) compared to the 25%

AC composite, which shows that the incorporation of SF in the cement composite generates modification in the hydration products formed.

4.5. Failure Prognosis of Embedded SCC in Beams.

Figures 18(a)–18(c) depict the deformation and failure of the flexural beam under a two-point load at the end of 28 days of curing. The maximum deflections of the beam are 21.764 mm at the flexure and 11.86 mm in the combined flexural-shear zone, respectively. At 18.7 kN, the beam develops its first flexural crack, whereas its maximum load-bearing capability is 96 kN due to the development of internal bending stress [61]. The flexural crack develops as the load increases. As illustrated in Figure 18(a), the flexural shear crack develops due to coupled flexural shear stress as the load increases progressively. As depicted in Figure 18(b),

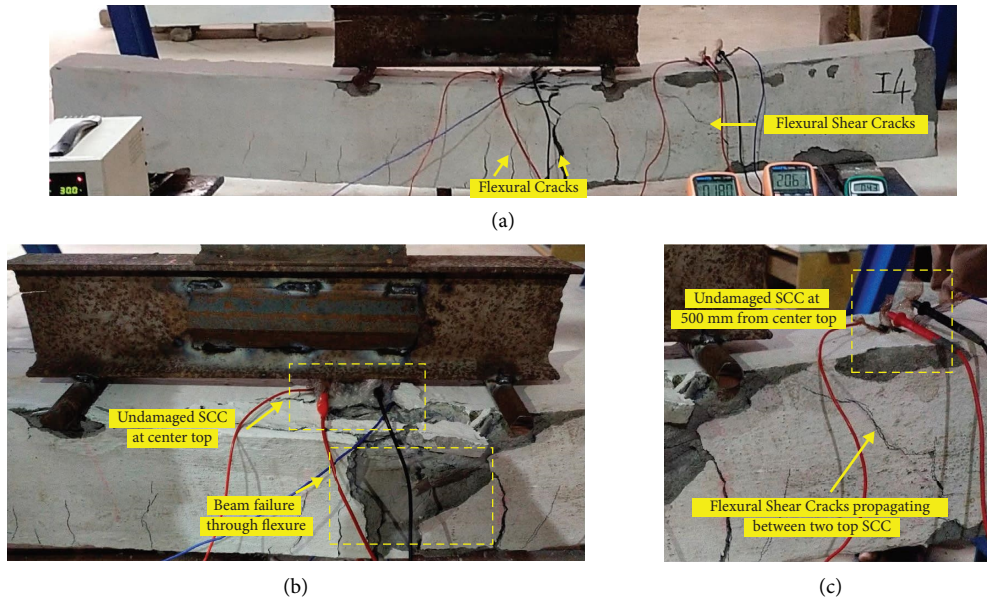


FIGURE 18: Real-time image of a damaged flexural beam with embedded SCC incorporating AC, demonstrating (a) the formation of flexural cracks and flexural shear cracks in the beams, (b) unbroken SCC at the bottom of the beam with beam failure due to flexure, and (c) intact SCC at 500 mm from the center top of the beam with flexural cracks propagating between two SCC embedded at beam top.

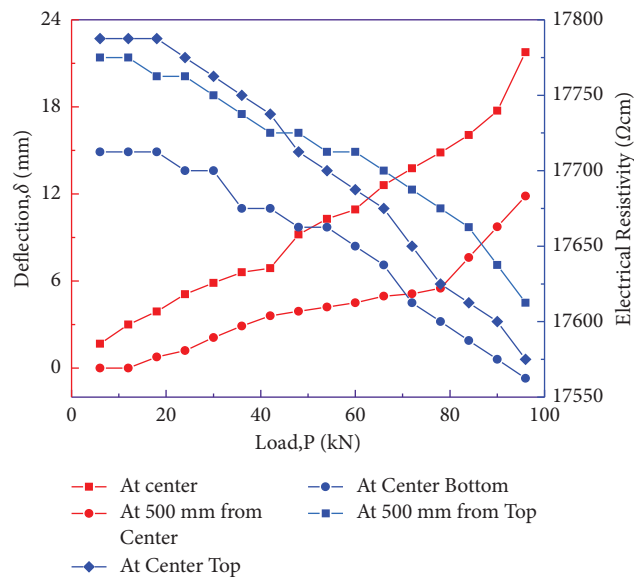


FIGURE 19: Load vs. deflection of the reinforced concrete beam with load vs. electrical resistivity of embedded SCC at center top, center bottom, and 500 mm from the center top of the beam.

the beam fails in flexure at its ultimate stress. Even though the beam fails in flexure, as seen in Figure 18(b), the SCC embedded at the top of the beam is unharmed. Similarly, flexural shear cracks occurred between the SCC embedded at the uniaxial tension and flexural-shear zone, resulting in undamaged SCC in the combined flexural-shear zone. Since the SCC is not affected by external stresses, they can monitor the deflection of the beam until the beam fails.

Figure 19 depicts the fluctuation in electrical resistivity concerning the load of SCC embedded at the various zones in the beam. The change in beam deflection at the flexure

and the flexural-shear zone is also shown in Figure 19. The center deflection rises from 1.676 mm to 17.737 mm when the beam is loaded from 6 kN to 90 kN. However, under compression, the SCC resistivity (100 Ωcm) does not change until 18 kN. This demonstrates that, despite the compression in SCC, the AC contained in SCC does not undergo any convergence within the SCC. This might be due to AC agglomerating together in high concentrations [17]. It is worth noting that the deflection at 500 mm from the center did not deflect until 12 kN, and the deflection at 18 kN is just 0.76 mm. This might also be explained by the

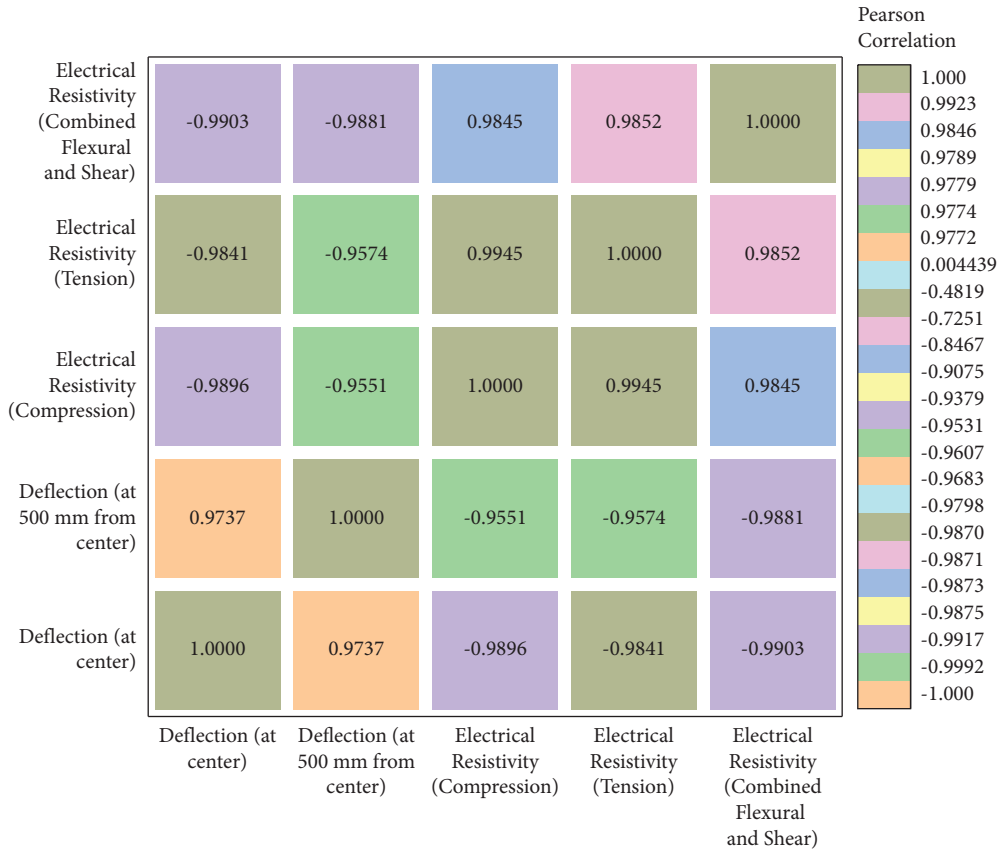


FIGURE 20: Pearson correlation coefficients between deflection of the beam (at the center, at 500 mm from the center) and electrical resistivity of SCC embedded (at tension, compression, combined flexure, and shear) in beams.

unchanging resistivity of SCC in the compression zone of the beam.

However, after 18 kN, the resistivity of SCC in compression is altered from 100 Ωcm (18 kN) to 21.05 Ωcm (90 kN). Beyond 90 kN, the deflection abruptly increases from 17.737 mm to 21.764 mm. As demonstrated in Figure 19, the SCC inserted at the compression zone dramatically reduces resistivity from 21.05 Ωcm to 10.53 Ωcm. However, due to changes in deflection, the resistivity of the SCC embedded in the stress zone does not vary significantly. With the rise in beam deflection from 1.676 mm to 21.764 mm, the change in resistivity of SCC in the stress zone has linearly decreased from 100 Ωcm to 7.69 Ωcm. This shows that the AC in the SCC has undergone no or fair minor deformations under tension, resulting in only a minor difference in resistivity. As a result, the SCC inserted in the compression zone clearly indicates beam deflection and can reveal a quick shift in resistivity when the deflection is abruptly changed. On the other hand, the SCC embedded in the tensile stress zone does not have a clear sign of change in beam deflection.

The deflection at 500 mm from the center of the beam increases from 0 mm to 5.5 mm as the load increases from 6 kN to 78 kN. At the same time, the electrical resistivity is lowered from 100 Ωcm (at 6 kN) to 46.67 Ωcm (at 78 kN), as

shown in Figure 19. Beyond 78 kN, the deflection of the beam at 500 mm from the center drops sharply from 5.5 mm (78 kN) to 11.86 mm (96 kN). Similarly, the electrical resistivity of SCC in the combined flexural and shear zone changes dramatically from 46.67 Ωcm to 13.33 Ωcm due to the convergence of AC in the embedded SCC [46]. The resistivity of the SCC in the combined flexure and shear zone can decrease as deflection lowers, and it can also display an abrupt fluctuation in resistivity when deflection drops suddenly. As a result, in the combined flexure and shear zone, the SCC with AC may be able to detect beam deformation.

The correlation between beam deflection (at the center, 500 mm from the center) and electrical resistivity of SCC integrated (at tension, compression, combined flexure, and shear) in beams is shown in Figure 20. The resistivity of SCC integrated into the compression zone exhibits a Pearson correlation with the deflection of the beam at the center and 500 mm from the center of the beam of roughly 98% and 97%, respectively. The electrical resistivity of the SCC integrated in the stress zone correlates with the deflection of the beam at the center and 500 mm from the beam center by about 99% and 98%, respectively. The electrical resistivity of the SCC integrated in the combined flexural and shear zone contributes more than 99% and 98% of the beam deflection at the center and 500 mm from the center of the beam, respectively.

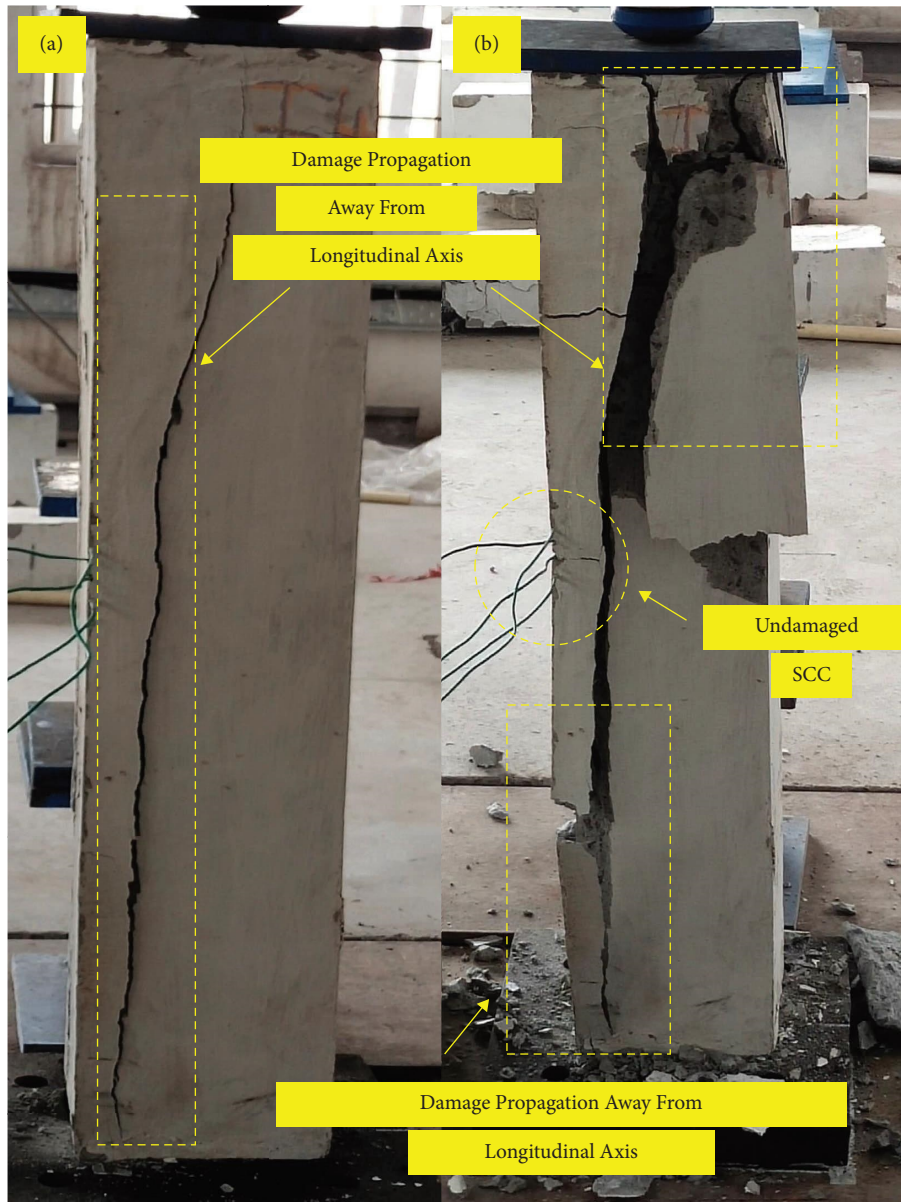


FIGURE 21: Real-time image of a failed concrete column with embedded SCC integrating AC, showing (a) concrete damage propagation away from the longitudinal axis of the column and (b) undamaged SCC at column center with crack penetration away from SCC.

4.6. Failure Prognosis of Embedded SCC in Columns. Figures 21(a) and 21(b) depict the deformation, crack pattern, and failure of a reinforced concrete column under axial load. The column has a maximum load-bearing capacity of 354 kN and a central deflection of 15.67 mm. As observed in Figure 21(a), the column collapses due to the formation of longitudinal cracks that propagate in the longitudinal direction but away from the longitudinal axis of the column due to the attainment of maximum load-carrying capacity. The SCC is unaffected by the collapse of the column because the crack propagates away from the longitudinal axis, as seen in Figure 21(b).

The variation in column deflection and resistivity of SCC as a function of the load on a concrete column is shown in Figure 22. The deflection of the beam increased

from 1.95 mm to 15.67 mm as the load increased from 20 kN to 354 kN. As depicted in Figure 22, the electrical resistivity of SCC has been reduced from 15350 Ωcm (at 20 kN) to 13462.5 Ωcm (at 354 kN). This is due to external force compressing the SCC in the column, forcing the AC in the SCC to touch each other. Contact and tunneling conduction are aided by the AC in the composite, lowering the resistivity of the composite [62]. Since the SCC is unaffected by column failure, the electrical resistivity of the SCC has a significant connection with column deflection.

As shown in Figure 23, the variation of column deflection has about 96% Pearson correlation with the electrical resistivity variation of SCC integrated with columns.

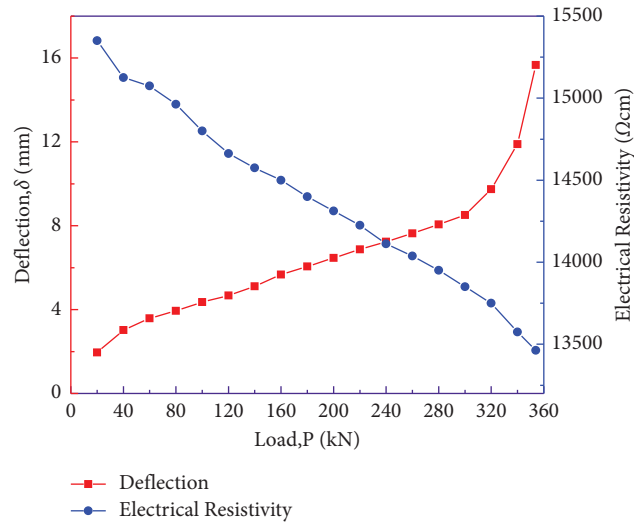


FIGURE 22: Load vs. deflection of a reinforced concrete column with load vs. electrical resistivity of an integrated SCC at the center of the column.

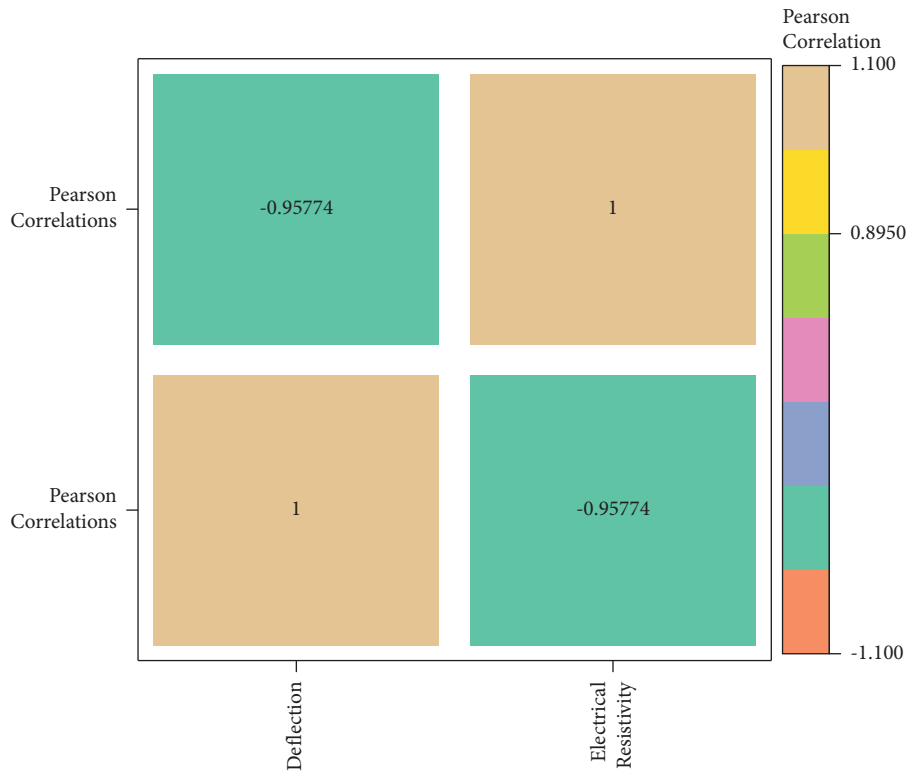


FIGURE 23: Pearson correlation coefficients between deflection of the column and resistivity of SCC embedded in columns.

5. Conclusion

The objective of this research is to design, optimize, and characterize SCC using AC and AC-SF. The developed and optimized SCC is embedded in beams and columns to monitor its deflection. The study led to the following conclusions:

- (1) The compressive strength of the SCC diminishes as the amount of AC in the composite increases. The 25% AC inclusion in the composite had the greatest loss in compressive strength (about 43.2%), while the

25% AC-SF composite had just a 30.19% reduction. The strength of the SCC is reduced due to the absorption capacities of AC. The AC absorbs water and adheres to the surface of the cement, delaying the hydration process. When 10% SF is added to all composites, the compressive strength increases in both AC and non-AC composites.

- (2) The development of a three-dimensional conductive network of AC results in a maximum decrease in resistivity of 46.20% at 25% AC. AC-SF composites,

- on the other hand, achieve a reduction of 40.76%. The AC and AC-SF embedded composites have 15% and 20% percolation thresholds, respectively.
- (3) For 25% AC and 15% AC-SF, the most significant decrease in FCR (5.70% and 8.18%) is obtained. The decrease in FCR is associated with the formation of contact and tunneling conduction as a result of the reduction in the distance between adjacent ACs in the composite. Even at the lesser stress increment, the excess concentration of AC contributes significantly to the FCR reduction in the composite. However, 5% AC reduced the FCR only to 4.63%, but it can reduce the resistivity to 14 MPa.
 - (4) The maximum stress sensitivity is achieved as 1.1% for 25% AC embedded cement composite. This is because, in addition to cluster formation (as seen in 5% AC), a continuous conductive chain arises in a 25% AC embedded composite (due to the high concentration), resulting in a significant increase in the sensitivity of the composite when compared to other concentrations. The stress sensitivity of 20% AC-SF composite is roughly 0.7% due to the substantial dispersion of AC by SF and the considerable contribution of contact and tunneling conduction to reducing resistivity at lower stress levels.
 - (5) Since the composite requires multifunctional properties, a new approach for optimizing the SCC is required. A performance index approach, a management tool that integrates many data types, is adopted to produce the SCC. The optimum % inclusions for strength, conductivity, piezoresistivity, and stress sensitivity are 25 AC and 20 AC-SF, respectively.
 - (6) According to SEM analysis, dense spacing of AC deposition improves the conductivity of the composite. EDAX reveals the concentration of Si, Ca, Fe, and Al content in the composite, which undergoes a chemical reaction to generate hydration products (C-S-H), contributing to the compressive strength of the composite. The AC embedded composite has high C content, which adds to the increased conductivity of the composite. XRD examination confirms the presence of C-S-H, portlandite, and ettringite in the composite, suggesting the explanation for the higher strength of the composite.
 - (7) When the deflection is rapidly changed, the SCC placed in the compression zone clearly indicates beam deflection and can disclose a fast shift in resistivity. In contrast, the SCC implanted in the tensile stress zone exhibits no sign of variation in beam deflection. The resistivity of the SCC integrated in the stress zone is 99% and 98% correlated with the deflection of the beam at the center and 500 mm from the beam center, respectively.
 - (8) Since the SCC is unaffected by column failure, the change in column deflection has a 96% Pearson correlation with the change in electrical resistivity of SCC integrated with columns.
- As a result, the developed multifunctional cement composite containing AC has high electromechanical properties and may be used to monitor the deflection of beams and columns.

Data Availability

The data that support the findings of this study are available within the article.

Conflicts of Interest

The authors declare that they have no conflicts of interest.

Authors' Contributions

A. Dinesh was involved in conceptualization, methodology, visualization, investigation, supervision, validation, and writing the original draft, D. Suji was involved in conceptualization and supervision, and M. Pichumani was involved in conceptualization, methodology, supervision, and writing, reviewing, and editing.

Acknowledgments

The authors would like to express their gratitude to the management, Sri Ramakrishna Engineering College, Coimbatore, India, for granting the SEED fund for this research.

References

- [1] S. Taheri, "A review on five key sensors for monitoring of concrete structures," *Construction and Building Materials*, vol. 204, pp. 492–509, 2019.
- [2] M. Zhiliang, L. Bin, and C. Wenjian, "An integrated approach for managing cladding construction in high-rise buildings," *Automation in Construction*, vol. 11, no. 5, pp. 545–555, 2002.
- [3] X. Tan, A. Abu-obeidah, Y. Bao, H. Nassif, and W. Nasreddine, "Measurement and visualization of strains and cracks in CFRP post-tensioned fiber reinforced concrete beams using distributed fiber optic sensors," *Automation in Construction*, vol. 124, Article ID 103604, 2021.
- [4] D. García and D. Tcherniak, "An experimental study on the data-driven structural health monitoring of large wind turbine blades using a single accelerometer and actuator," *Mechanical Systems and Signal Processing*, vol. 127, pp. 102–119, 2019.
- [5] V. Talakokula, Vaibhav, and S. Bhalla, "Non-destructive strength evaluation of fly ash based geopolymer concrete using piezo sensors," *Procedia Engineering*, vol. 145, pp. 1029–1035, 2016.
- [6] A. Barrias, J. R. Casas, and S. Villalba, "Fatigue performance of distributed optical fiber sensors in reinforced concrete elements," *Construction and Building Materials*, vol. 218, pp. 214–223, 2019.

- [7] Z. Dong, J. Zhang, X. Ma, and H. Zhao, "Measurement accuracy analysis of distributed fiber optic sensors for asphalt mixture based on the dem-fdm coupled method," *Structural Control and Health Monitoring*, vol. 2023, Article ID 4093158, 16 pages, 2023.
- [8] S. C. Mukhopadhyay and I. Ihara, "Sensors and technologies for structural health monitoring: a review bt - new developments in sensing Technology for structural health monitoring," *Lecture Notes in Electrical Engineering*, vol. 96, pp. 1–14, 2011.
- [9] S. Ding, Y. Ruan, X. Yu, B. Han, and Y. Q. Ni, "Self-monitoring of smart concrete column incorporating CNT/NCB composite fillers modified cementitious sensors," *Construction and Building Materials*, vol. 201, pp. 127–137, 2019.
- [10] S. Ding, Y. Xiang, Y. Q. Ni et al., "In-situ synthesizing carbon nanotubes on cement to develop self-sensing cementitious composites for smart high-speed rail infrastructures," *Nano Today*, vol. 43, Article ID 101438, 2022.
- [11] B. del Moral, F. J. Baeza, R. Navarro et al., "Temperature and humidity influence on the strain sensing performance of hybrid carbon nanotubes and graphite cement composites," *Construction and Building Materials*, vol. 284, Article ID 122786, 2021.
- [12] M. K. Kim, J. Park, and D. J. Kim, "Characterizing the electro-mechanical response of self-sensing steel-fiber-reinforced cementitious composites," *Construction and Building Materials*, vol. 240, Article ID 117954, 2020.
- [13] M. Pichumani and M. Pichumani, "Electro-mechanical investigations of steel fiber reinforced self-sensing cement composite and their implications for real-time structural health monitoring," *Journal of Building Engineering*, vol. 51, Article ID 104343, 2022.
- [14] A. Dinesh, D. Suji, and M. Pichumani, "Development of a comprehensive methodology for the design and fabrication of carbon fiber integrated cement composite toward health monitoring of structural components," *Engineering Structures*, vol. 277, Article ID 115453, 2023.
- [15] A. Dinesh, D. Suji, and M. Pichumani, "Sensors and Actuators a . Physical Self-sensing cementitious composite sensor with integrated steel fiber and carbonaceous powder for real-time application in large-scale infrastructures," *Sensors and Actuators A: Physical*, vol. 353, Article ID 114209, 2023.
- [16] B. Han, X. Yu, and J. Ou, *Self-Sensing Concrete in Smart Structures*, Elsevier, Amsterdam, Netherlands, 2014.
- [17] B. Han, S. Ding, and X. Yu, "Intrinsic self-sensing concrete and structures: a review," *Measurement*, vol. 59, pp. 110–128, 2015.
- [18] J. Diaz-escobar, D. Paulina, S. Venkataraman, and D. Arnoldo, "Classification and characterization of damage in composite laminates using electrical resistance tomography and supervised machine learning," *Structural Control and Health Monitoring*, vol. 2023, Article ID 1675867, 19 pages, 2023.
- [19] S. Beskhyroun, L. D. Wegner, and B. F. Sparling, "Integral resonant control scheme for cancelling human-induced vibrations in light-weight pedestrian structures," *Structural Control and Health Monitoring*, vol. 19, no. 1, 2011.
- [20] S. J. Lee, I. You, S. Kim, H. O. Shin, and D. Y. Yoo, "Self-sensing capacity of ultra-high-performance fiber-reinforced concrete containing conductive powders in tension," *Cement and Concrete Composites*, vol. 125, Article ID 104331, 2022.
- [21] C. G. Berrocal, K. Hornbostel, M. R. Geiker, I. Löfgren, K. Lundgren, and D. G. Bekas, "Electrical resistivity measurements in steel fibre reinforced cementitious materials," *Cement and Concrete Composites*, vol. 89, pp. 216–229, 2018.
- [22] A. O. Monteiro, P. B. Cachim, and P. M. F. J. Costa, "Electrical properties of cement-based composites containing carbon black particles," *Materials Today Proceedings*, vol. 2, no. 1, pp. 193–199, 2015.
- [23] B. Han and J. Ou, "Embedded piezoresistive cement-based stress/strain sensor," *Sensors and Actuators A: Physical*, vol. 138, no. 2, pp. 294–298, 2007.
- [24] S. Wen and D. D. L. Chung, "Partial replacement of carbon fiber by carbon black in multifunctional cement-matrix composites," *Carbon*, vol. 45, no. 3, pp. 505–513, 2007.
- [25] W. Li, W. Dong, L. Shen, A. Castel, and S. P. Shah, "Conductivity and piezoresistivity of nano-carbon black (NCB) enhanced functional cement-based sensors using polypropylene fibres," *Materials Letters*, vol. 270, Article ID 127736, 2020.
- [26] M. Houari, B. Hamdi, O. Bouras, J. C. Bollinger, and M. Baudu, "Static sorption of phenol and 4-nitrophenol onto composite geomaterials based on montmorillonite, activated carbon and cement," *Chemical Engineering Journal*, vol. 255, pp. 506–512, 2014.
- [27] M. Aime, "Effects of contamination by drilling muds," *Oil*, vol. 195, pp. 225–233, 1952.
- [28] M. Horgnies, I. Dubois-Brugger, and E. M. Gartner, "NO x de-pollution by hardened concrete and the influence of activated charcoal additions," *Cement and Concrete Research*, vol. 42, no. 10, pp. 1348–1355, 2012.
- [29] I. Justo-Reinoso, A. Caicedo-Ramirez, W. V. Srubar, and M. T. Hernandez, "Fine aggregate substitution with acidified granular activated carbon influences fresh-state and mechanical properties of ordinary Portland cement mortars," *Construction and Building Materials*, vol. 207, pp. 59–69, 2019.
- [30] M. Horgnies, F. Serre, I. Dubois-brugger, and E. Gartner, "NOx de - pollution using activated charcoal concrete - from laboratory experiments to tests with prototype garages," *Cement and Concrete Research*, vol. 42, pp. 1348–1355, 2014.
- [31] M. Mahoutian, A. S. Lubell, and V. S. Bindiganavile, "Effect of powdered activated carbon on the air void characteristics of concrete containing fly ash," *Construction and Building Materials*, vol. 80, pp. 84–91, 2015.
- [32] C. Zheng, Z. Liu, J. Xu, X. Li, and Y. Yao, "Compressive strength and microstructure of activated carbon-fly ash cement composites," *Chemical Engineering Transactions*, vol. 59, pp. 475–480, 2017.
- [33] M. Frías, R. Vigil de la Villa, R. García, S. Martínez, E. Villar, and I. Vegas, "Effect of a high content in activated carbon waste on low clinker cement microstructure and properties," *Construction and Building Materials*, vol. 184, pp. 11–19, 2018.
- [34] W. Dong, W. Li, L. Shen, and D. Sheng, "Piezoresistive behaviours of carbon black cement-based sensors with layer-distributed conductive rubber fibres," *Materials & Design*, vol. 182, Article ID 108012, 2019.
- [35] I. Justo-Reinoso, W. V. Srubar, A. Caicedo-Ramirez, and M. T. Hernandez, "Fine aggregate substitution by granular activated carbon can improve physical and mechanical properties of cement mortars," *Construction and Building Materials*, vol. 164, pp. 750–759, 2018.
- [36] M. M. Karimi, H. Jahanbakhsh, B. Jahangiri, and F. Moghadas Nejad, "Induced heating-healing characterization of activated carbon modified asphalt concrete under microwave

- radiation,” *Construction and Building Materials*, vol. 178, pp. 254–271, 2018.
- [37] C. O. Chin, X. Yang, S. C. Paul, Susilawati, L. S. Wong, and S. Y. Kong, “Development of thermal energy storage lightweight concrete using paraffin-oil palm kernel shell-activated carbon composite,” *Journal of Cleaner Production*, vol. 261, Article ID 121227, 2020.
- [38] J. Huang, D. D. Koroteev, and M. Zhang, “Smartphone-based study of cement-activated charcoal coatings for removal of organic pollutants from water,” *Construction and Building Materials*, vol. 300, Article ID 124034, 2021.
- [39] C. O. Chin, X. Yang, S. Y. Kong, S. C. Paul, Susilawati, and L. S. Wong, “Mechanical and thermal properties of lightweight concrete incorporated with activated carbon as coarse aggregate,” *Journal of Building Engineering*, vol. 31, Article ID 101347, 2020.
- [40] Tran-SET, *Influence of Powder Activated Carbon (PAC) in Fly Ash on the Properties of Concrete*, Transportation Consortium of South-Central States, Shreveport, LA, USA, 2020.
- [41] H. A. Arafat, V. M. Hebatpuria, H. S. Rho, N. G. Pinto, P. L. Bishop, and R. C. Buchanan, “Immobilization of phenol in cement-based solidified/stabilized hazardous wastes using regenerated activated carbon: role of carbon,” *Journal of Hazardous Materials*, vol. 70, no. 3, pp. 139–156, 1999.
- [42] B. Chowdhury, “Investigations into the role of activated carbon in a moisture-blocking cement formulation,” *Journal of Thermal Analysis and Calorimetry*, vol. 78, no. 1, pp. 215–226, 2004.
- [43] F. Aslani, A. Dehghani, and L. Wang, “The effect of hollow glass microspheres, carbon nanofibers and activated carbon powder on mechanical and dry shrinkage performance of ultra-lightweight engineered cementitious composites,” *Construction and Building Materials*, vol. 280, Article ID 122415, 2021.
- [44] X. Zhou, Y. Wang, C. Gong, B. Liu, and G. Wei, “Production, structural design, functional control, and broad applications of carbon nanofiber-based nanomaterials: a comprehensive review,” *Chemical Engineering Journal*, vol. 402, Article ID 126189, 2020.
- [45] Y. He, L. Lu, S. Jin, and S. Hu, “Conductive aggregate prepared using graphite and clay and its use in conductive mortar,” *Construction and Building Materials*, vol. 53, pp. 131–137, 2014.
- [46] H. Xiao, H. Li, and J. Ou, “Strain sensing properties of cement-based sensors embedded at various stress zones in a bending concrete beam,” *Sensors and Actuators A: Physical*, vol. 167, no. 2, pp. 581–587, 2011.
- [47] X. Li and M. Li, “Multifunctional self-sensing and ductile cementitious materials,” *Cement and Concrete Research*, vol. 123, Article ID 105714, 2019.
- [48] A. O. Monteiro, P. B. Cachim, and P. M. F. J. Costa, “Self-sensing piezoresistive cement composite loaded with carbon black particles,” *Cement and Concrete Composites*, vol. 81, pp. 59–65, 2017.
- [49] S. H. Liu, M. Q. Wu, M. J. Rao, L. H. Li, and H. L. Xiao, “Preparation, properties, and microstructure of graphite powder-containing conductive concrete,” *Strength of Materials*, vol. 51, no. 1, pp. 76–84, 2019.
- [50] I. Papanikolaou, C. Litina, A. Zomorodian, and A. Al-Tabbaa, “Effect of natural graphite fineness on the performance and electrical conductivity of cement paste mixes for self-sensing structures,” *Materials*, vol. 13, no. 24, pp. 5833–5919, 2020.
- [51] X. Fan, D. Fang, M. Sun, and Z. Li, “Piezoresistivity of carbon fiber graphite cement-based composites with CCCW,” *Journal of Wuhan University of Technology-Materials Science Edition*, vol. 26, no. 2, pp. 339–343, 2011.
- [52] X. Liu and S. Wu, “Study on the graphite and carbon fiber modified asphalt concrete,” *Construction and Building Materials*, vol. 25, no. 4, pp. 1807–1811, 2011.
- [53] S. Wu, L. Mo, Z. Shui, and Z. Chen, “Investigation of the conductivity of asphalt concrete containing conductive fillers,” *Carbon*, vol. 43, no. 7, pp. 1358–1363, 2005.
- [54] H. Li, H. g. Xiao, and J. p. Ou, “Effect of compressive strain on electrical resistivity of carbon black-filled cement-based composites,” *Cement and Concrete Composites*, vol. 28, no. 9, pp. 824–828, 2006.
- [55] A. Dehghani and F. Aslani, “The effect of shape memory alloy, steel, and carbon fibres on fresh, mechanical, and electrical properties of self-compacting cementitious composites,” *Cement and Concrete Composites*, vol. 112, Article ID 103659, 2020.
- [56] S. Y. Lee, H. V. Le, and D. J. Kim, “Self-stress sensing smart concrete containing fine steel slag aggregates and steel fibers under high compressive stress,” *Construction and Building Materials*, vol. 220, pp. 149–160, 2019.
- [57] Y. Huang, H. Li, and S. Qian, “Self-sensing properties of engineered cementitious composites,” *Construction and Building Materials*, vol. 174, pp. 253–262, 2018.
- [58] A. S. El-Dieb, M. A. El-Ghareeb, M. A. H. Abdel-Rahman, and E. S. A. Nasr, “Multifunctional electrically conductive concrete using different fillers,” *Journal of Building Engineering*, vol. 15, pp. 61–69, 2018.
- [59] F. J. Baeza, O. Galao, E. Zornoza, and P. Garcés, “Multifunctional cement composites strain and damage sensors applied on reinforced concrete (RC) structural elements,” *Materials*, vol. 6, no. 3, pp. 841–855, 2013.
- [60] W. Zeng, Y. Ding, Y. Zhang, and F. Dehn, “Effect of steel fiber on the crack permeability evolution and crack surface topography of concrete subjected to freeze-thaw damage,” *Cement and Concrete Research*, vol. 138, Article ID 106230, 2020.
- [61] P. Bhatt and M. A. Kader, “Prediction of shear strength of reinforced concrete beams by nonlinear finite element analysis,” *Computers & Structures*, vol. 68, no. 1–3, pp. 139–155, 1998.
- [62] O. A. Mendoza Reales and R. Dias Toledo Filho, “A review on the chemical, mechanical and microstructural characterization of carbon nanotubes-cement based composites,” *Construction and Building Materials*, vol. 154, pp. 697–710, 2017.